

Phase-segregated Pt–Ni chain-like nanohybrids with high electrocatalytic activity towards methanol oxidation reaction†

Cite this: *Nanoscale*, 2014, 6, 4635

Li-Li Wang, Dong-Feng Zhang* and Lin Guo*

The phase-segregated Pt–Ni chain-like nanostructures, composed of monometallic counterparts attached to each other, were synthesized *via* a modified polyol process with the assistance of a small amount of PVP. The molar ratio between Pt and Ni was tuned by simply adjusting the feed ratio of the precursors. High-resolution transmission electron microscopy (HR-TEM) and X-ray photoelectron spectroscopy (XPS) results reveal that atomic diffusion occurred at the interface of the granular subunits. The negative shift of the Pt4f_{7/2} peak in the XPS spectra indicates the electron transfer from Ni to Pt atoms, while the strong peaks at around 855.7 eV suggest the surface oxidation of the Ni nanoparticles, which was further confirmed by the cyclic voltammetry (CV) measurement. The electrocatalytic activities of the methanol oxidation reaction (MOR) were found to be higher for the phase-segregated structures relative to those for pure Pt nanoparticles, and the activities followed the sequences of Pt₁Ni₁ > Pt₃Ni₁ ~ Pt₂Ni₃ > pure Pt. We believe that the modified electronic structures and the existence of nickel hydroxide both contributed to the improved catalytic activities.

Received 9th January 2014
Accepted 4th February 2014

DOI: 10.1039/c4nr00139g

www.rsc.org/nanoscale

Introduction

Direct methanol fuel cells (DMFCs), with the advantages of high energy conversion efficiency, safe storage and less pollution, are expected as one of the promising candidates used in small portable electronic products. Platinum is still the most effective anode electrocatalyst towards the methanol oxidation reaction (MOR). However, the high cost and low tolerance to carbon monoxide (CO) of pure Pt catalysts are the main drawbacks hindering the widespread application of this technology.^{1–3}

Since researchers found that deposition of Pt nanoparticles on transition metals (TMs) could significantly enhance the CO tolerance and considerably improve the catalytic activity of MOR,^{4–6} Pt-based bimetallic catalysts have received great research attention. An electronic effect was proposed to explain the enhancement. The theory deems that the d-band position of Pt is lowered owing to the modified electronic structure by the electron transfer from the TM substrates to the Pt overlayers.^{7–9} According to the Hammer–Nørskov model, the binding energy of CO on the metallic catalyst is proportional to the d-band center of the surface atoms.^{10,11} Thus, it is reasonable to expect the weakened adsorption of CO on Pt with the downshifted d-band center. Furthermore, studies also revealed that the

monolayer-dispersed Pt on the substrate would maximize the electronic modification.^{7,12}

The amazing results triggered the research on Pt-based bimetallic nanoalloys^{13–16} to mimic the electronic and catalytic properties established on extended surfaces. Further research shows that besides the electronic effect between TM and Pt, the existence of TM hydroxides might also play an important role in improving the electrocatalytic activity towards MOR, because the hydroxides have high electronic conductivity and can innately express OH species to remove the Pt-adsorbed CO.^{17–19}

However, the alloy structure will inevitably block the formation of the hydroxide.²⁰ Hence, in the past several years, there has been a debate on which is more important for the improved performance, alloying or the existence of hydroxide.^{21–23} For example, Lu and co-workers²⁴ showed that both increasing the content of hydrous ruthenium oxides and decreasing the particle size increase the catalytic activity, whereas the effect of the alloy degree turned out to be unremarkable. Long *et al.*²⁰ even proposed that avoiding the formation of PtRu bimetallic alloys could make the catalysts more active for MOR, because they believed that the RuO_xH_y speciation in nanoscaled Pt–Ru blacks afforded much more active sites than Ru⁰ did as part of the bimetallic alloy. Park and coworkers also attributed isolated monometallic NPs as the active composition in Pt–Ni²⁵ and Pt–Co²⁶ nanohybrids for CO PROX. Inspired by these results, it is reasonable to conclude that a structure containing both intimately interacted Pt–TM interface and TM hydroxides would have optimized catalytic activity.

School of Chemistry and Environment, Beihang University, Beijing 100191, PR China.
E-mail: dfzhang@buaa.edu.cn; guolin@buaa.edu.cn

† Electronic supplementary information (ESI) available. See DOI: 10.1039/c4nr00139g

In addition, most Pt-based bimetallic nanocatalysts have been prepared using organometallic precursors (such as acetylacetonate) in a high-boiling organic solvent until now.^{27–29} On the one hand, they would cause great harm to both the human body and the environment. On the other hand, the residue from these organic molecules, which cannot be easily removed, might block the surface reactive sites and thus deactivate the catalyst.^{30,31}

By sharing this insight, we report the fabrication of phase-segregated Pt–Ni chain-like structures composed of nanoscaled monometallic counterparts attached to each other in ethylene glycol solution with the assistance of a small amount of polyvinyl pyrrolidone (PVP). The atomic diffusion at the interface guaranteed the modification of the electronic structure of Pt *via* electron transfer, while the phase-segregated structure made it possible to generate sufficient nickel hydroxides. The electrochemical measurement confirms that the phase-segregated structures possessed much higher catalytic activities towards MOR relative to pure Pt nanocatalysts.

Experimental

The phase-segregated Pt–Ni bimetallic nanocrystals were prepared through a separated reduction procedure *via* a modified polyol process. Ethylene glycol served as both the reducing agent and the solvent. Typically, 0.0292 g K_2PtCl_6 and 0.0260 g PVP were dissolved into 30 mL ethylene glycol. Then, an appropriate amount of $\text{NiCl}_2 \cdot 6\text{H}_2\text{O}$ was introduced into the above mixture to obtain bimetallic nanocrystals with different Pt/Ni molar ratios. After stirring for 30 minutes, a homogeneous transparent solution formed. After the temperature was raised to the boiling point ($\sim 190^\circ\text{C}$), 3.0 mL solution containing 0.2 mL 80% hydrazine hydrate ($\text{N}_2\text{H}_4 \cdot \text{H}_2\text{O}$) and 2.8 mL ethylene glycol was added into the above mixture. It was allowed to reflux for 2 hours to complete the reaction. After the mixture was cooled to room temperature, the produced precipitates were collected by centrifugation and washed with ethanol several times. All the experimental procedures were performed open to the atmosphere and all the reagents were used without further purification.

The crystalline structures of the as-synthesized products were analyzed by X-ray diffraction (XRD) and recorded on a Rigaku D/max-2200 diffractometer employing Cu-K α radiation ($\lambda = 1.54056 \text{ \AA}$) at a scanning rate of $0.01^\circ \text{ s}^{-1}$ ranging from 30 to 90° . The morphologies were investigated by transmission electron microscopy (TEM) and high-resolution TEM (HR-TEM) on a JEOL instrument (JEM-2100F) working at 200 kV. The composition of the as-synthesized Pt–Ni nanocatalysts was characterized by energy dispersive X-ray spectroscopy (EDX) equipped within a JEM-2100F TEM. XPS analyses were performed on an AXIS-Ultra instrument using monochromatic Al K α radiation with 1486.71 eV operating at 15 kV and 225 W. To compensate for surface charge effects, binding energies were calibrated using the C 1s hydrocarbon peak at 284.80 eV.

The electrochemical measurements were performed in a standard three-electrode cell at room temperature conducted

with a CHI660C electrochemical workstation (Chenhua, Shanghai). Pt wire was used as the counter electrode and an Ag/AgCl electrode saturated with KCl was used as the reference electrode. The working electrode was prepared as follows. An aliquot of $5 \mu\text{L}$ of 2 mg mL^{-1} as-synthesized nanocatalyst suspension in deionized water was dropped onto the glassy carbon electrode (3 mm in diameter), which was polished smoothly and washed cleanly in advance. After the water evaporated completely, $5 \mu\text{L}$ of 0.2 mol L^{-1} Nafion as a binding agent was cast on the top of the catalyst layer. The coated working electrode was then dried completely in air. The cyclic voltammetry (CV) measurements were carried out in the aqueous solution of $0.5 \text{ mol L}^{-1} \text{ H}_2\text{SO}_4$ with or without $1 \text{ mol L}^{-1} \text{ CH}_3\text{OH}$ for different purposes. Chronoamperometry measurements were performed under a potential of 0.7 V for 600 s in $0.5 \text{ mol L}^{-1} \text{ H}_2\text{SO}_4 + 1.0 \text{ mol L}^{-1} \text{ CH}_3\text{OH}$ solution. All solutions were fully purged with Ar gas before the measurements.

Results and discussion

The phase-segregated Pt–Ni bimetallic nanohybrids with an adjusted molar ratio were prepared through a separated reduction procedure *via* a modified polyol process. Fig. 1(a) to (c) display the typical TEM images of the as-synthesized products with different Pt/Ni atomic ratios. Table S1† illustrates that the average Pt/Ni atomic ratios in different electrocatalysts were 2.89 : 1, 1.15 : 1 and 0.63 : 1, approaching to the average molar ratio of Pt/Ni as 3 : 1, 1 : 1 and 2 : 3 (denoted as Pt_3Ni_1 , Pt_1Ni_1 and Pt_2Ni_3 in the context below), respectively. It can be seen that regardless of the Pt/Ni atomic ratios, all the products exhibited chain-like structures composed of near-spherical nanoparticles attached to each other with mean diameters of 4–5 nm, which tended to cross-link into networks. As shown in Fig. 1(d), the three samples (Pt_3Ni_1 , Pt_1Ni_1 and Pt_2Ni_3) possessed similar X-ray diffraction (XRD) patterns, which can be indexed to the face-centered-cubic (fcc) phase. Rather surprisingly, no obvious peak shift was identified relative to the XRD pattern of the pure Pt

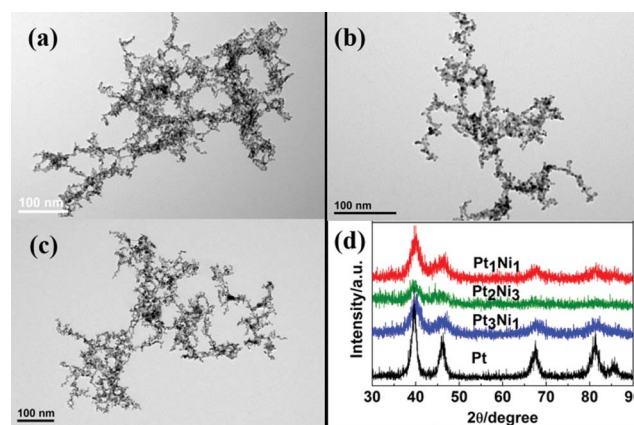


Fig. 1 Broad view TEM images of (a) Pt_3Ni_1 , (b) Pt_1Ni_1 , and (c) Pt_2Ni_3 , and (d) the corresponding XRD patterns of Pt–Ni nanohybrids of various compositions and pure Pt nanoparticles produced by a similar procedure.

nanoparticles obtained using a similar process except for the introduction of the Ni precursor, which excludes the possibility of the alloyed structures. However, the diffractions from Ni were not observed. The “fluorescence effect” might contribute to the absence of the signal from Ni in the XRD pattern. It is known that the fluorescence effect exists for elements one to five places left of the target material in the periodic table. Cu-K α radiation is employed during the XRD characterization in our case, thus the strong fluorescence would lead to the high background to block the signals from Ni.

To figure out their detailed configurations, HRTEM measurement was employed. Fig. 2(a) to (f) show the typical HRTEM images of Pt₃Ni₁, Pt₁Ni₁ and Pt₂Ni₃, respectively. The clearly identified grain boundary provides solid evidence for the nature of nanoparticle attachment. The lattice fringes with spaces of 0.226 and 0.203 nm can be identified in all cases, consistent with (111) planes of fcc-Pt (JCPDS 04-0802) and fcc-Ni (JCPDS 04-0850),³² respectively. That is to say that the nanochains were assembled by the attachment of phase-segregated Pt and Ni nanoparticles instead of Pt–Ni nanoalloys. After detailed analysis, configuration schematic diagrams were built to illustrate the corresponding composition distribution of the chains in the images. They indicate that the Pt and Ni nanoparticles were arranged in a random manner. Much closer observation reveals that the nanoparticles were not attached physically, but interfacial fusion had occurred both among the homogeneous-particles (Pt–Pt and Ni–Ni) and among the heterogeneous-particles (Pt–Ni) as demonstrated by the enlarged images recorded on the interfacial regions. Thus, it is reasonable to infer that the Pt and Ni subunits might share a mixed interface or there might exist a small number of Pt–Ni bonds in the products despite the phase-segregated structural feature. The interfacial atomic diffusion is not out of expectation since the alloying ability between Ni and Pt is extremely strong.^{13,33}

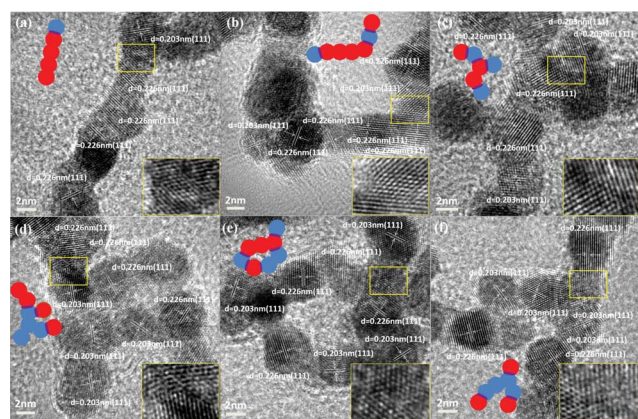
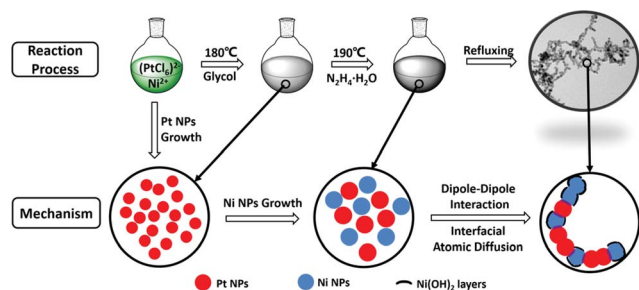


Fig. 2 The HR-TEM images of (a and b) Pt₃Ni₁, (c and d) Pt₁Ni₁, and (e and f) Pt₂Ni₃. The inserted schematic diagrams illustrate the configuration of Pt and Ni, with red and blue balls representing Pt and Ni particles, respectively. The inserts at the lower right corner of each HRTEM image are the corresponding amplified images recorded at the yellow framed regions, showing the detailed structure information at the Pt–Ni interfacial area.

Then, it gives rise to another question on why the phase-segregated structure rather than the alloy was generated. In our case, the color of the reaction solution turned into black at about 180 °C before the introduction of hydrazine hydrate (N₂H₄·H₂O). TEM and EDS characterization results reveal that the products collected at this stage mainly consisted of Pt nanoparticles (as shown in Fig. S2 in the ESI†). Considering the much higher standard reduction potential of PtCl₆^{2−}/Pt ($E^\theta = 0.375$ eV vs. SHE) than that of Ni²⁺/Ni ($E^\theta = -0.25$ eV vs. SHE), it is easy to understand that ethylene glycol is a weak reducer. It is known that hydrazine hydrate (N₂H₄·H₂O) is a kind of strong reducing agent. Under refluxing, the introduction of N₂H₄·H₂O led to continuous growth of Pt and fast nucleation and growth of Ni. Ni must have grown into nanoparticles before the Ni atoms had sufficient time to diffuse into the lattice of Pt. The separated nucleation-growth process for Pt and Ni produced the phase-segregated nanoparticles. The insufficient energy at relatively low reaction temperatures (<200 °C) might be another possible reason to restrain the bulk alloying. The failure to obtain a pure Pt chain-like structure in the absence of NiCl₂ as shown in Fig. S1† indicates that Ni played a critical role on the growth of the chain-like structure. We believe that it was the dipole–dipole interaction that worked. For magnetic Ni nanoparticles, they behaved like magnetic dipoles, which also induced the dipoles of the neighboring Pt nanoparticles. The strong and long range dipole–dipole interactions³⁴ organized the nanoparticles together. The linear arrangement is believed to maximize the attraction of opposite magnetic poles.³⁵ Under refluxing, the interfacial atomic diffusion was facilitated, which made the adjacent particles fuse into each other and thus the chain-like structures were stabilized. The control experiment indicated that without the addition of PVP, the products exhibited as aggregates composed of irregular particles with sizes as large as ~50 nm (see Fig. S3 in the ESI†). It is not out of the expectation since PVP was reported as the classical surfactant to prevent the agglomeration of the nanoparticles.^{36,37} Scheme 1 depicts the formation mechanism of the phase-segregated Pt–Ni chain-like nanohybrids.

To further examine the surface characteristics of the nanohybrids with different Pt/Ni atomic ratios, XPS measurements were performed. As can be seen from the curves 1–3 in Fig. 3(a), the Pt4f core-level spectra of the three samples all consisted of two peaks for metallic platinum centered at ~71 (Pt4f_{7/2}) and ~74 eV (Pt4f_{5/2}), respectively. No Pt²⁺- and Pt⁴⁺-related peaks were observed. The metallic Pt is believed to provide more active sites for methanol oxidation than ionic Pt species.³⁸ It is worth noting that in comparison with the pure Pt nanoparticles, the Pt4f core-level peaks of the as-prepared nanohybrids all shifted towards the lower binding energy side, with the negative shifts of about 0.18, 0.45 and 0.40 eV for Pt₃Ni₁, Pt₁Ni₁ and Pt₂Ni₃, respectively. In conjunction with the HR-TEM and XRD results, we can conclude that the electron transfer between Pt and Ni occurred owing to the atomic diffusion at the interfaces. Due to the electronegativity difference between Pt (2.28) and Ni (1.91), the electron shift from Ni to Pt led to the downshift of the d-band center of Pt and thus the lowered binding energy.



Scheme 1 The schematic illustration of the formation mechanism of the phase-segregated Pt–Ni chain-like nanohybrids.

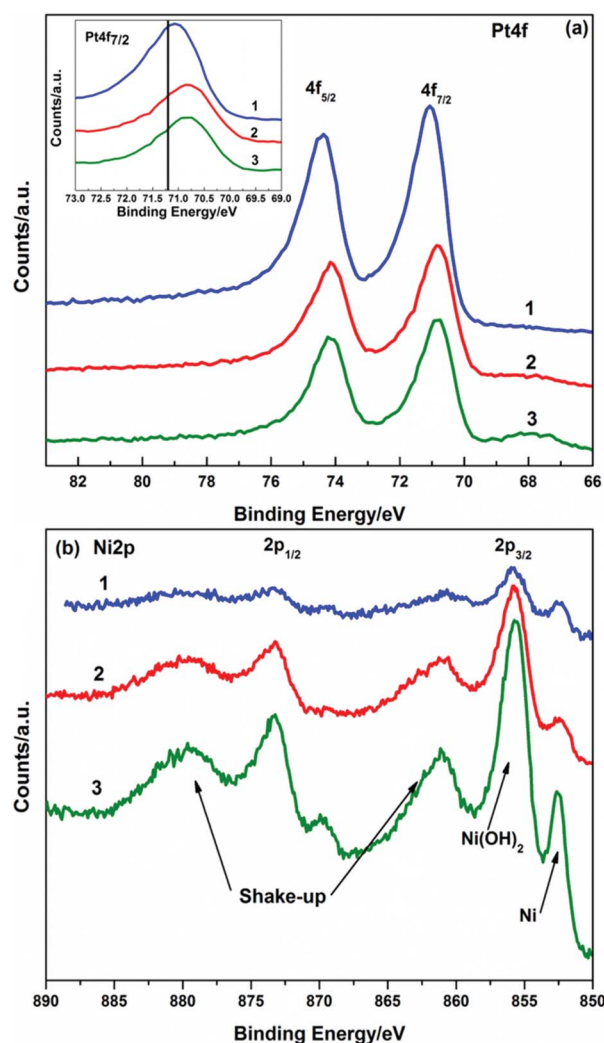


Fig. 3 XPS spectra of Pt–Ni nanohybrids: spectra 1 to 3 correspond to Pt_1Ni_1 , Pt_3Ni_1 , and Pt_2Ni_3 , respectively. (a) Pt 4f and (b) Ni 2p.

Obviously, the larger Pt–Ni interfacial area would facilitate the electron transfer. Since the contact possibility between Pt and Ni would be maximized when Pt : Ni approaches 1 : 1, the Pt 4f core-level peaks of Pt_1Ni_1 and Pt_2Ni_3 would be expected to shift more negatively than Pt_3Ni_1 , consistent with the experimental data in our case.

The Ni2p spectra of the nanohybrids are shown in Fig. 3(b). Generally, the structure of the Ni2p core-level spectra is complicated because of the presence of the broad satellite peaks (~ 860.9 eV and ~ 879.9 eV) adjacent to the main peaks, which are attributed to multi-electron excitation. Besides the shake-up peaks, both metallic Ni-related and $\text{Ni}(\text{OH})_2$ -related peaks can be clearly identified. According to the well-documented data,³⁹ the peaks at 852.5 eV are originated from metallic Ni and the peaks at 855.7 eV can be assigned to $\text{Ni}(\text{OH})_2$. To further confirm the existence of $\text{Ni}(\text{OH})_2$, we performed the cyclic voltammetry (CV) measurement in aqueous alkaline solutions. Typical electrochemical redox peaks are expected owing to the electrochemical reaction between $\text{Ni}(\text{OH})_2$ and NiOOH according to the following equation:

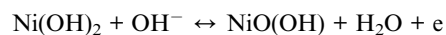


Fig. S4 in the ESI† shows the CV curves of the Pt_2Ni_3 nanohybrids. The CV curves exhibit a broad cathodic current peak at around 0.3 V and an anodic current peak at around 0.4 V (vs. Ag/AgCl). The anodic current peak is related to the oxidation of nickel hydroxide to nickel oxyhydroxide while the cathodic one is associated with the reduced conversion of oxyhydroxide back to nickel hydroxide.⁴⁰

The electrocatalytic performance of the as-prepared Pt–Ni nanocatalysts towards MOR was studied by electrochemical cyclic voltammetry and chronoamperometry. For comparison, the pure Pt catalyst synthesized by a similar process as shown in Fig. S1† was also examined. Fig. 4(a) shows the CV curve of the as-prepared nanocatalysts recorded in $0.5 \text{ mol L}^{-1} \text{ H}_2\text{SO}_4$ without methanol from -0.2 V to 1.0 V at a sweep rate of 50 mV s^{-1} . The electrocatalytic currents were normalized to the mass of Pt. The curves of the nanohybrids are similar to those of the pure Pt nanoparticles, showing well-defined hydrogen adsorption/desorption peaks in the potential region of -0.2 V to 0.2 V, the double-layer region from 0.20 to 0.40 V, and the metal oxidation/reduction peaks in the range of 0.4 V to 0.8 V. The electrochemically active surface area (EASA) was calculated on the basis of the integrated hydrogen desorption area, according to the equation $\text{EASA} = Q_{\text{H}} / (Q_{\text{monolayer}}^{\text{H}} \times W_{\text{Pt}})$, where Q_{H} is the total charge (μC) for hydrogen desorption, $Q_{\text{monolayer}}^{\text{H}}$ represents the charge density involved in hydrogen monolayer desorption from a smooth Pt surface ($210 \mu\text{C cm}^{-2}$) and W_{Pt} represents the Pt loading on the electrode.⁴¹ The EASA values of Pt_3Ni_1 , Pt_1Ni_1 , Pt_2Ni_3 and pure Pt nanocatalysts were 13, 24, 9 and $5 \text{ m}^2 \text{ g}^{-1}$, respectively. The integrated hydrogen adsorption area shows that the EASA values of Pt_3Ni_1 , Pt_1Ni_1 , and Pt_2Ni_3 were all higher than that of pure Pt, indicating more electrochemical active sites with the addition of Ni.

Fig. 4(b) shows the typical CV curves of methanol electro-oxidation on Pt-based catalysts tested in aqueous solution containing $0.5 \text{ mol L}^{-1} \text{ H}_2\text{SO}_4 + 1 \text{ mol L}^{-1} \text{ CH}_3\text{OH}$. The overall shapes of the cyclic voltammograms were in good agreement with the previous literature. At potentials below 0.20 V, the oxidation current was negligible in all voltammograms because

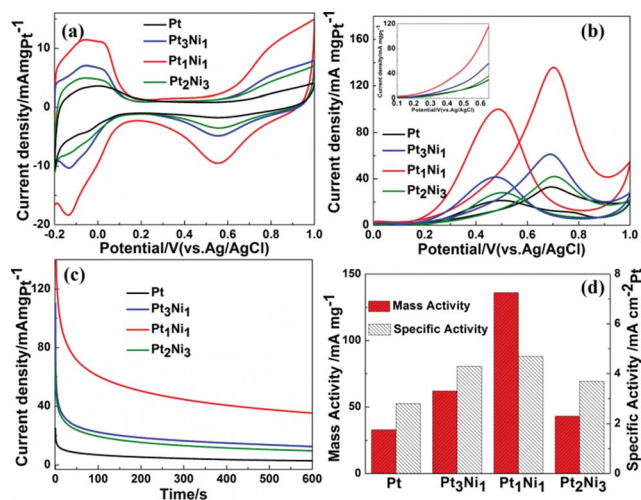


Fig. 4 Cyclic voltammograms of Pt–Ni nanohybrids in (a) 0.5 mol L⁻¹ H₂SO₄ and (b) 0.5 mol L⁻¹ H₂SO₄ + 1 mol L⁻¹ CH₃OH, (c) chronoamperometry curves of Pt–Ni nanohybrids in 0.5 mol L⁻¹ H₂SO₄ + 1 mol L⁻¹ CH₃OH at 0.7 V and (d) comparison of mass and area specific activities of the four catalysts for methanol oxidation. The inset in (b) is the amplified part of the CVs at a low potential range. The scanning rate in all the cases is 50 mV s⁻¹.

the surface Pt active sites were poisoned by CO_{ads}, an intermediate from dehydrogenation of methanol. With the potential increasing, the methanol oxidation began and well-defined anodic peaks were observed at about 0.70 V in the forward sweep. The onset potential of methanol oxidation and the forward anodic peak potential are the two major parameters to evaluate the catalytic performance.^{42,43} As can be seen in the inset of Fig. 4(b) and Table 1, the onset potentials with the as-prepared Pt–Ni nanohybrids as the catalysts were all lower than that of the pure Pt, suggesting that it was more favorable for methanol oxidation. Ni in the Pt-based catalysts is believed to significantly lower the onset potential through the synergistic effect, in which the adsorption of oxygenous species occurred at much lower potential on the additive Ni than that on Pt. The anodic peak current was also enhanced by the addition of Ni. The mass-normalized current density (as shown in Fig. 4(d)) of the anodic peak on Pt₁Ni₁ nanocatalysts (136 mA mg_{Pt}⁻¹) was higher than those on Pt₃Ni₁ (62 mA mg_{Pt}⁻¹) and Pt₂Ni₃ (43 mA mg_{Pt}⁻¹) and as high as about 4 times of pure Pt (33 mA mg_{Pt}⁻¹). The area-normalized specific peak current density (as shown in Fig. S5† and 4(d)) of the Pt₁Ni₁ nanocatalysts (4.7 mA cm⁻²) was also higher than those of Pt₃Ni₁ (4.3 mA cm⁻²) and Pt₂Ni₃ (3.7 mA cm⁻²), and was about 2 times higher than that of pure Pt (2.8 mA cm⁻²). The

results indicate that the addition of Ni enhanced the electrochemical activity of Pt.

Furthermore, the long-term stability and tolerant ability to CO intermediates were evaluated by the chronoamperometry measurements performed in 0.5 mol L⁻¹ H₂SO₄ + 1 mol L⁻¹ CH₃OH at 0.70 V. As shown in Fig. 4(c), the current densities of all catalysts decayed rapidly at the initial stage, which might be due to the hydrogen adsorption and the double-layer discharge. The subsequent decay was believed to be caused by the adsorption of a small amount of CO on the catalyst surfaces during methanol electrooxidation.⁴⁴ Although the current continued to decay gradually, the nanohybrids all maintained a higher current density (normalized to the mass of Pt) than the pure Pt over the entire time range, demonstrating the prominent stability and tolerance to CO. Among the three samples, Pt₁Ni₁ exhibited the slowest current decay over time, confirming its excellent electrocatalytic performance.

Obviously, the phase-segregated Pt–Ni chain-like nanohybrids in our case were highly beneficial as anodic electrocatalysts for MOR relative to pure Pt, benefited by the following three aspects: (a) the lowered onset potential for the methanol oxidation reaction; (b) the higher mass activity and specific activity towards the methanol oxidation; (c) the enhanced long-term stability and resistance to CO poisoning. On the whole, the catalytic activities toward MOR followed the sequence of Pt₁Ni₁ > Pt₂Ni₃ ~ Pt₃Ni₁ > pure Pt. The enhanced electrocatalytic performance probably could be attributed to the so-called bifunctional mechanism. According to the XPS results, the electronic structure of Pt was modified by the electron transfer from Ni to Pt, which led to the downshifted d-band center of Pt and thus reduced the adsorption energies of CO on Pt. The existence of Ni(OH)₂ layers on the catalysts was also believed to play an important role in the improvement of the catalytic activity. It was reported that the OH species produced from the hydroxide layer could react with the CO_{ads} species on the Pt particles. The process can be described as the following equation: NiOH_{ads} + PtCO_{ads} → CO₂ + Pt + Ni + H⁺ + e⁻.^{18,45} The desorption of CO_{ads} could recover the active sites on Pt. However, excess Ni loading would also lower the catalytic activity since the excess surface occupation by Ni would decrease the available Pt for MOR. The combination of the lowered d-band center and the efficient active sites endowed the Pt₁Ni₁ with the best catalytic performance.

Conclusions

The phase-segregated Pt–Ni chain-like nanohybrids were synthesized *via* a modified polyol process with the assistance of

Table 1 Comparison of the catalytic activity of the Pt–Ni catalysts for methanol oxidation

Catalyst	EASA/m ² g ⁻¹	Onset potential/V	Specific activity/mA cm ⁻²	Mass activity/mA mg _{Pt} ⁻¹
Pt	13	0.39	2.8	33
Pt ₃ Ni ₁	24	0.29	4.3	62
Pt ₁ Ni ₁	9	0.25	4.7	136
Pt ₂ Ni ₃	5	0.34	3.7	43

a small amount of PVP. HRTEM characterization shows that the nanohybrids were composed of Ni and Pt nanoparticles attached to each other in a random manner with interfacial atomic fusion. The separated nucleation-growth process for Pt and Ni and the relative low reaction temperature prevented the diffusion of Ni atoms into the bulk Pt, which guaranteed the phase-segregated structure. The dipole-dipole interaction was believed to be responsible for the formation of the chain-like structure. XPS results reveal the modified electron structure of Pt owing to the charge transfer from Ni at the interfacial region. The electrocatalytic performance of MOR was evaluated by cyclic voltammetry and chronoamperometry. The nanohybrids exhibit both higher electrocatalytic activities and improved CO tolerance relative to the pure Pt nanoparticles synthesized under similar conditions. The activity and the stability both followed the sequences of $\text{Pt}_1\text{Ni}_1 > \text{Pt}_3\text{Ni}_1 \sim \text{Pt}_2\text{Ni}_3 \gg \text{pure Pt}$. We believe that the modified electronic structures and the existence of nickel hydroxide both contributed to the improved electrocatalytic performance.

Acknowledgements

The project was supported by the National Natural Science Foundation of China (21173015) and the National Key Basic Research Program of China (973) (2010CB934700).

Notes and references

- G. A. Somorjai, *Chem. Rev.*, 1996, **96**, 1223–1235.
- H. Zhang, M. Jin and Y. Xia, *Chem. Soc. Rev.*, 2012, **41**, 8035–8049.
- S. H. Noh, M. H. Seo, J. K. Seo, P. Fischer and B. Han, *Nanoscale*, 2013, **5**, 8625–8633.
- S. R. Brankovic, J. McBreen and R. R. Adzic, *Surf. Sci.*, 2001, **479**, L363–L368.
- S. R. Brankovic, J. X. Wang, Y. Zhu, R. Sabatini, J. McBreen and R. R. Adzic, *J. Electroanal. Chem.*, 2002, **524**, 231–241.
- K. Sasaki, Y. Mo, J. X. Wang, M. Balasubramanian, F. Uribe, J. McBreen and R. R. Adzic, *Electrochim. Acta*, 2003, **48**, 3841–3849.
- A. Schlappa, M. Lischka, A. Groß, U. Käsberger and P. Jakob, *Phys. Rev. Lett.*, 2003, **91**, 016101.
- V. R. Stamenkovic, B. Fowler, B. S. Mun, G. Wang, P. N. Ross, C. A. Lucas and N. M. Markovic, *Science*, 2007, **315**, 493–497.
- T. G. Kelly and J. G. Chen, *Chem. Soc. Rev.*, 2012, **41**, 8021–8034.
- B. Hammer, L. B. Hansen and J. K. Nørskov, *Phys. Rev. B: Condens. Matter Mater. Phys.*, 1999, **59**, 7413–7421.
- W. Du, Q. Wang, D. Saxner, N. A. Deskins, D. Su, J. E. Krzanowski, A. I. Frenkel and X. Teng, *J. Am. Chem. Soc.*, 2011, **133**, 15172–15183.
- D. V. Esposito, S. T. Hunt, Y. C. Kimmel and J. G. Chen, *J. Am. Chem. Soc.*, 2012, **134**, 3025–3033.
- T. C. Deivaraj, W. Chen and J. Y. Lee, *J. Mater. Chem.*, 2003, **13**, 2555.
- X. Teng, S. Maksimuk, S. Frommer and H. Yang, *Chem. Mater.*, 2007, **19**, 36–41.
- C. Wang, D. van der Vliet, K. L. More, N. J. Zaluzec, S. Peng, S. Sun, H. Daimon, G. Wang, J. Greeley, J. Pearson, A. P. Paulikas, G. Karapetrov, D. Strmcnik, N. M. Markovic and V. R. Stamenkovic, *Nano Lett.*, 2011, **11**, 919–926.
- J. Suntivich, Z. Xu, C. E. Carlton, J. Kim, B. Han, S. W. Lee, N. Bonnet, N. Marzari, L. F. Allard, H. A. Gasteiger, K. Hamad-Schifferli and Y. Shao-Horn, *J. Am. Chem. Soc.*, 2013, **135**, 7985–7991.
- C. Xu, P. k. Shen and Y. Liu, *J. Power Sources*, 2007, **164**, 527–531.
- E. Formo, Z. Peng, E. Lee, X. Lu, H. Yang and Y. Xia, *J. Phys. Chem. C*, 2008, **112**, 9970–9975.
- J. J. Pietron, M. B. Pomfret, C. N. Chervin, J. W. Long and D. R. Rolison, *J. Mater. Chem.*, 2012, **22**, 5197.
- J. W. Long, R. M. Stroud, K. E. Swider-Lyons and D. R. Rolison, *J. Phys. Chem. B*, 2000, **104**, 9772–9776.
- M. Inoue, T. Nishimura, S. Akamaru, A. Taguchi, M. Umeda and T. Abe, *Electrochim. Acta*, 2009, **54**, 4764–4771.
- R. Mu, Q. Fu, H. Xu, H. Zhang, Y. Huang, Z. Jiang, S. Zhang, D. Tan and X. Bao, *J. Am. Chem. Soc.*, 2011, **133**, 1978–1986.
- D. Wu, Z. Zheng, S. Gao, M. Cao and R. Cao, *Phys. Chem. Chem. Phys.*, 2012, **14**, 8051–8057.
- Q. Y. Lu, B. Yang, L. Zhuang and J. T. Lu, *J. Phys. Chem. B*, 2005, **109**, 8873–8879.
- E.-Y. Ko, E. D. Park, K. W. Seo, H. C. Lee, D. Lee and S. Kim, *Catal. Lett.*, 2006, **110**, 275–279.
- E. Y. Ko, E. D. Park, H. C. Lee, D. Lee and S. Kim, *Angew. Chem., Int. Ed. Engl.*, 2007, **46**, 734–737.
- C. Wang, N. M. Markovic and V. R. Stamenkovic, *ACS Catal.*, 2012, **2**, 891–898.
- C. Wang, M. Chi, G. Wang, D. van der Vliet, D. Li, K. More, H.-H. Wang, J. A. Schlueter, N. M. Markovic and V. R. Stamenkovic, *Adv. Funct. Mater.*, 2011, **21**, 147–152.
- C. Wang, M. Chi, D. Li, D. Strmcnik, D. van der Vliet, G. Wang, V. Komanicky, K. C. Chang, A. P. Paulikas, D. Tripkovic, J. Pearson, K. L. More, N. M. Markovic and V. R. Stamenkovic, *J. Am. Chem. Soc.*, 2011, **133**, 14396–14403.
- M. Chen, B. Wu, J. Yang and N. Zheng, *Adv. Mater.*, 2012, **24**, 862–879.
- H. Chen, D. Wang, Y. Yu, K. A. Newton, D. A. Muller, H. Abruna and F. J. DiSalvo, *J. Am. Chem. Soc.*, 2012, **134**, 18453–18459.
- X. Huang, E. Zhu, Y. Chen, Y. Li, C. Y. Chiu, Y. Xu, Z. Lin, X. Duan and Y. Huang, *Adv. Mater.*, 2013, **25**, 2974–2979.
- J. Zhang, H. Yang, J. Fang and S. Zou, *Nano Lett.*, 2010, **10**, 638–644.
- S. A. Iakovenko, A. S. Trifonov, M. Giersig, A. Mamedov, D. K. Nagesha, V. V. Hanin, E. C. Soldatov and N. A. Kotov, *Adv. Mater.*, 1999, **11**, 388–392.
- Z. Tang, N. A. Kotov and M. Giersig, *Science*, 2002, **297**, 237–240.
- Y. Xiong, I. Washio, J. Chen, H. Cai, Z.-Y. Li and Y. Xia, *Langmuir*, 2006, **22**, 8563–8570.
- O. D. Lyons, N. E. Musselwhite, L. M. Carl, K. A. Manbeck and A. L. Marsh, *Langmuir*, 2010, **26**, 16481–16485.

- 38 Y. Hu, P. Wu, Y. Yin, H. Zhang and C. Cai, *Appl. Catal., B*, 2012, **111–112**, 208–217.
- 39 T.-Y. Jeon, S. J. Yoo, Y.-H. Cho, K.-S. Lee, S. H. Kang and Y.-E. Sung, *J. Phys. Chem. C*, 2009, **113**, 19732–19739.
- 40 K. Watanabe, T. Kikuoka and N. Kumagai, *J. Appl. Electrochem.*, 1995, **25**, 219–226.
- 41 A. C. Ferrandez, S. Baranton, J. Bigarre, P. Buvat and C. Coutanceau, *Langmuir*, 2012, **28**, 17832–17840.
- 42 Z. Zhang, Y. Wang and X. Wang, *Nanoscale*, 2011, **3**, 1663–1674.
- 43 J. Xu, X. Liu, Y. Chen, Y. Zhou, T. Lu and Y. Tang, *J. Mater. Chem.*, 2012, **22**, 23659.
- 44 L. X. Ding, A. L. Wang, G. R. Li, Z. Q. Liu, W. X. Zhao, C. Y. Su and Y. X. Tong, *J. Am. Chem. Soc.*, 2012, **134**, 5730–5733.
- 45 B. Habibi and E. Dadashpour, *Int. J. Hydrogen Energy*, 2013, **38**, 5425–5434.